Scripta Materialia 237 (2023) 115705

Contents lists available at ScienceDirect

Scripta Materialia

journal homepage: www.journals.elsevier.com/scripta-materialia

Mechanisms of necklace recrystallization in a BCC Fe-Al-Ta alloy with strengthening Laves phase precipitates

Aliakbar Emdadi [a,*], Yitong Yang [a], Sebastian Bolz [b], Oleg Stryzhyboroda [c], Michael Tovar [d], Sergej Gein [c], Ulrike Hecht [c], Sabine Weiß [a]

[a] Chair of Physical Metallurgy and Materials Technology, Brandenburg University of Technology Cottbus-Senftenberg, Konrad-Wachsmann-Allee 17, Cottbus 03046, Germany

[b] Chair of Hybrid Manufacturing, Brandenburg University of Technology Cottbus-Senftenberg, Konrad-Wachsmann-Allee 17, Cottbus 03046, Germany

[c] Access e.V., Intzestr. 5, Aachen 52072, Germany

[d] Helmholtz-Zentrum Berlin für Materialien und Energie GmbH, Hahn-Meitner-Platz 1, Berlin 14109, Germany

ARTICLE INFO

Keywords:
Hot working
Iron aluminides
Dynamic recrystallization
Particle-stimulated nucleation (PSN)
Grain boundary migration

ABSTRACT

A necklace structure composed of fine grains formed by dynamic recrystallization was uncommonly observed at the pre-existing grain boundaries during the hot compression of a BCC Fe-25Al-1.5Ta alloy containing C14 - $(Fe, Al)_2Ta$ Laves phase precipitates. Two possible mechanisms for necklace formation were proposed; particle-stimulated nucleation and grain boundary bulging, depending on whether the original grain boundaries are occupied by C14 particles, or they are free of them. Recrystallization was initiated preferentially around the clusters of large particles at the boundaries containing particles. In contrast, the bulging of the original grain boundaries by strain-induced boundary migration was observed as a preliminary stage for necklace formation at the particle-free boundaries. The necklace structure expanded into the deformed volume in such a way that low-angle subgrain boundaries decorating the necklace layers transformed into grains with increasing deformation strain.

Dynamic softening (restoration) processes occur during deformation at high temperatures, which can significantly affect the microstructure and mechanical properties of the finished components [1]. Dynamic recrystallization (DRX) occurs mainly in face-centered cubic (FCC) metals and alloys having low or medium stacking fault energy (SFE). In such materials, recovery by the cross-slip of screw dislocations is suppressed [1]; therefore, the dislocation density significantly increases during deformation, providing the driving force for DRX. DRX typically originates at the pre-existing high-angle grain boundaries (GBs) and percolates into the unrecrystallized volume [2]. Bulging of original GBs through strain-induced boundary migration (SIBM) is frequently observed as a preliminary stage for DRX [3]. As the imposed deformation proceeds, the bulged boundaries eventually transform into equiaxed grains at the pre-existing GBs, leading to characteristic necklace structures [1,4].

In contrast, the occurrence of DRX is limited in both BCC metals and alloys and FCC metals and alloys of high SFE (such as aluminum and its alloys) since dislocation climb and cross-slip occur readily in those materials. Thus, the dislocation density (i.e., the driving force for DRX) is lowered, and the formation of the necklace structure is not often found in such materials. Dynamic recovery (DRV) is the primary flow softening mechanism in BCC metals and alloys, which reduces work hardening and leads to a steady-state regime. The microstructure developed by DRV during hot working consists of elongated deformed grains fragmented into subgrains enclosed with low-angle boundaries [1,5].

The primary softening mechanisms often reported for BCC Fe_3Al-based alloys during hot deformation within the A2-disordered αFe phase field include DRV, continuous DRX, and superplasticity [6–8], depending on the imposed deformation conditions. In an earlier study, DRV followed by recrystallization was observed for the Fe-25Al-1.5Ta alloy produced by spark plasma sintering [9]. As expected, due to the strong tendency of the BCC structure for DRV, the formation of fine recrystallized grains along the prior grain boundaries during hot deformation was rarely observed in Fe-25Al-1.5Ta alloys [10,11]. However, the formation mechanisms of the recrystallized grains were not investigated in those studies.

In the present study, it has been shown that discontinuous DRX takes place in BCC Fe-25Al-1.5Ta alloy containing Laves phase particles

* Corresponding author.
E-mail address: emdadi@b-tu.de (A. Emdadi).

https://doi.org/10.1016/j.scriptamat.2023.115705
Received 9 May 2023; Received in revised form 1 August 2023; Accepted 1 August 2023
Available online 4 August 2023

during deformation at 900 °C, leading to a necklace structure of recrystallized grains along the original GBs. This observation is unique because such a necklace DRX structure typically occurs in FCC metals and alloys with medium to low stacking fault energies [1,2,4,12–14] but rarely in BCC metals and alloys, including ferritic iron [15–17] and few BCC refractory high-entropy alloys [18–21].

Two possible mechanisms for necklace formation are proposed; particle-stimulated nucleation (PSN) and strain-induced bulging of original grain boundaries, depending on whether the original grain boundaries contain Laves phase particles or are free of them. The percolation mechanism of the necklace structure into the deformed volume will also be discussed based on direct observations.

An ingot of Fe-25Al-1.5Ta (at.%) alloy with a diameter of 30 mm and a length of 14 mm was fabricated by centrifugal investment casting from pure metals of the constituent elements by Access e.V. Aachen, Germany.

The phase identification was performed by a Bruker D8 ADVANCE diffractometer using Cu-K_α radiation. The as-cast specimen was heated to deformation temperature at a rate of ≈1 K/s in an Anton Paar HTK 1200 N oven. X-ray diffraction (XRD) was conducted at 900 °C within the 2θ range of 18–55° with a step size of 0.015° under a vacuum of 9.4 × 10^{-3} mbar. XRD was also performed at room temperature on the deformed samples within the 2θ range of 20–120° with a step size of 0.05°.

Cylindrical specimens with a diameter of 5 mm and a height of 8 mm were compressed at 900 °C up to a true strain of 0.8 with strain rates from 0.0013 s^{-1} to 0.1 s^{-1} under Ar atmosphere by a DIL805A/D/T dilatometer. The deformed specimens were cooled immediately after deformation to preserve the high-temperature microstructures.

A scanning electron microscope (SEM) TESCAN MIRA II equipped with a high-resolution electron backscatter diffraction (EBSD – EDAX system) detector was used for characterization.

Fig. 1(a) shows the true stress–true strain curves of the Fe-25Al-1.5Ta alloy samples hot compressed up to a true strain of 0.8 at 900 °C with different strain rates. The flow stress decreases with decreasing strain rate. The flow curves at 0.0013 s^{-1} and 0.01 s^{-1} show a broad flow stress peak followed by a slight decrease. This shape is typical for the occurrence of DRX in conventional BCC metals like α-iron, where a large stress drop in flow stress-strain curves was not observed despite the occurrence of DRX [15,16]. The stress peak is more distinct at the higher strain rate of 0.1 s^{-1}.

Fig. 1(b) displays the high-temperature XRD pattern of the studied alloy at 900 °C, showing a mixture of αFe (A2), FeAl (B2), and (Fe, Al)$_2$Ta (C14) phases at the deformation temperature. Fig. 1(c) shows that the B2 and C14 have been retained at room temperature after deformation and cooling. The B2 and C14 Laves phase are already present during hot compression at 900 °C and were not formed only during cooling after the deformation. It is worth mentioning that the B2 is insignificant at the deformation temperature since the transition temperature from B2-order to A2-disorder in the studied Fe-25Al-1.5Ta cast alloy was found to be in the range of 900–950 °C by differential scanning calorimetry (Fig. S1 in supplementary material). The B2 to A2 transformation temperature obtained in the present study agrees well with the literature [22]. The possible order effects on the deformation, recovery, and recrystallization will be discussed later. The C14 Laves phase precipitations mainly decorate the Fe-Al matrix GBs, as shown in the SEM images in Fig. 2(a) and (b). In addition to the particles located at the GBs, a small fraction of C14 particles is dispersed within the Fe-Al grains. The presence of Laves phase particles at the deformation temperature could lead to local deformation inhomogeneities that serve as potential nuclei near the pre-existing GBs, which will be investigated later.

Fig. 2(c)–(f) show SEM backscatter electron images of longitudinal cross-sections of the Fe-25Al-1.5Ta alloy specimens compressed up to a true strain of 0.8 at 900 °C with strain rates of 0.0013 s^{-1} and 1 s^{-1}. The material was subjected to slight or even no deformation in the areas

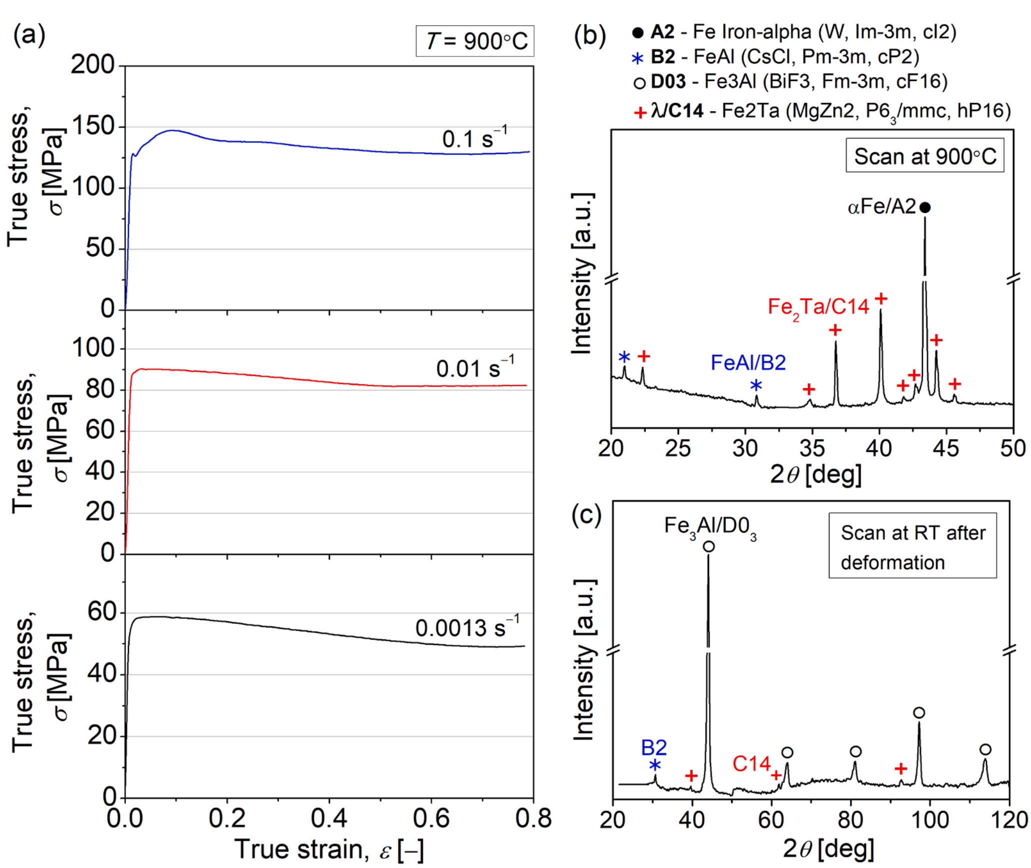

Fig. 1. True stress-strain curves for the Fe-25Al-1.5Ta alloy specimens hot compressed up to a true strain of 0.8 at 900 °C with different strain rates (a), XRD pattern at 900 °C (b) showing the presence of B2-FeAl and C14-(Fe, Al)$_2$Ta Laves phase precipitates at hot deformation temperature, and XRD pattern at room temperature after compression at 900 °C / 0.01 s^{-1} and air cooling (c) showing the B2 and Laves phase precipitates have been retained at room temperature after deformation and cooling.

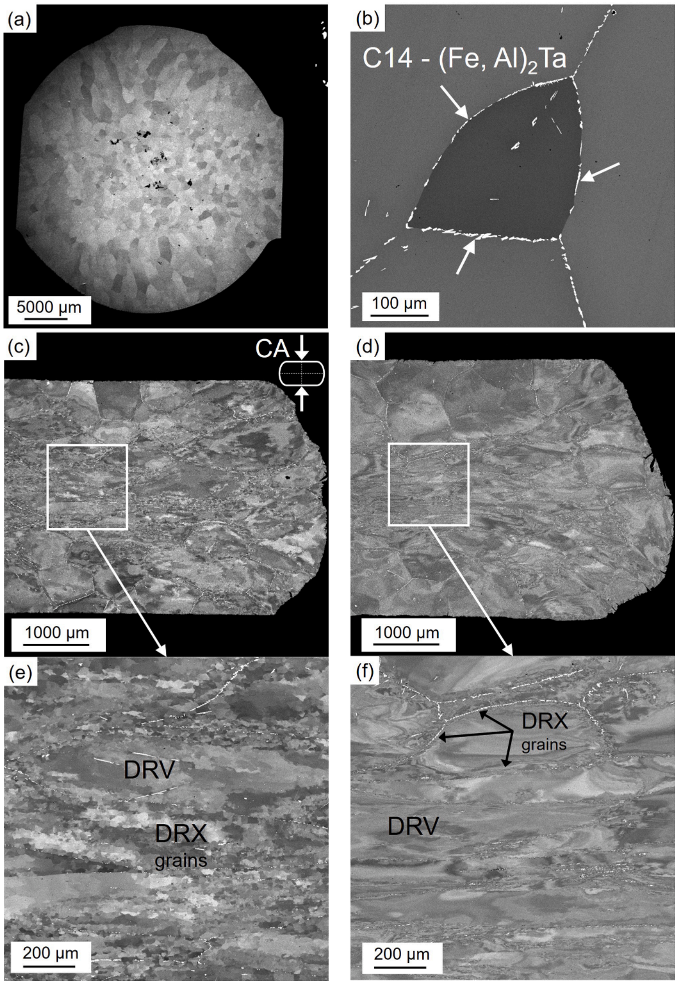

Fig. 2. Typical SEM-BSE micrographs of the Fe-25Al-1.5Ta specimens in as-cast (a and b) and hot compressed at 900 °C up to a true strain of 0.8 with a strain rate of 0.0013 s^{-1} (c and e) and 1 s^{-1} (d and f) states, showing elongated deformed grains with orientation gradients and substructures inside and a few small grains located close to the initial grain boundary regions. Arrows in (b) refer to some C14 Laves phase precipitates located mainly at the GBs. High-resolution views of the central regions of the deformed specimens marked by squares in (c) and (d) are shown in (e) and (f), respectively. The compression axis (CA) is vertical.

close to the forging dies (known as the dead metal zone). In contrast, deformation was localized mainly in the central region of the specimens, characterized by flat, heavily deformed grains elongated perpendicular to the compression axis (CA). No shear bands and intergranular cracks are observed, and only a few cavities are visible in the barreling areas. Higher magnification images in (c) and (d) show significant orientation gradients in the form of darker and lighter spots and/or curvy bands inside the deformed grains, indicating the annihilation of dislocations and their rearrangement into substructures, which is typical for the BCC metals and alloys where DRV takes place. In addition, a fine-grained structure is observed near and along the GBs, as shown in Fig. 2(e) and (f). These grains are bounded by HAGBs, as demonstrated by the EBSD maps in Fig. 3(a) and (b). Therefore, it can be concluded that these small grains are likely recrystallized grains forming necklace structures along the pre-existing GBs. Such behavior is not typical for the BCC metals and alloys and will be discussed later.

Evidence shows that the small recrystallized grains were mainly formed dynamically during hot deformation. Initially, the fraction and the size of the recrystallized grains increased with decreasing strain rate. Assuming they are recrystallized grains bounded by HAGBs, they cannot

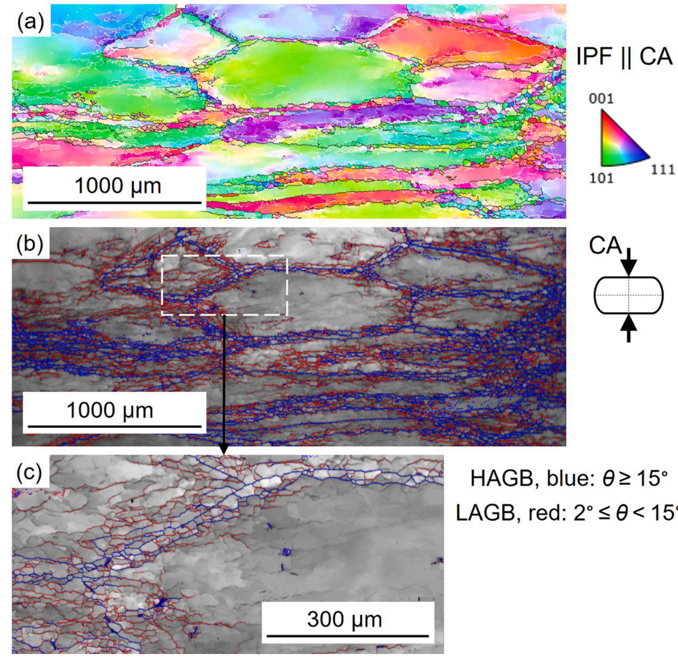

Fig. 3. EBSD inverse pole figure, IPF, (a) and image quality, IQ, (b) maps overlaid with grain boundary misorientations showing small grains enclosed with high-angle grain boundaries located close to the original grain boundary regions in the Fe-25Al-1.5Ta specimen hot compressed at 900 °C / 0.0013 s^{-1} to a true strain of 0.8. The red and blue lines mark low-angle grain boundaries (LAGBs) with misorientations (θ), $2^\circ \leq \theta < 15^\circ$ and high-angle grain boundaries (HAGBs) with $\theta \geq 15^\circ$, respectively. The IPF maps correspond to the orientations parallel to the compression axis (CA), which is vertical. The map in (c) shows a high-resolution view of the region outlined by a square in (b), showing substructures bounded by LAGBs within the recrystallized necklace grains. A high frequency of low-angle boundaries is also observed at the interface between the original, undeformed grains and finer recrystallized grains, as marked by red lines in (b) and (c). (For interpretation of the references to colour in this figure legend, the reader is referred to the web version of this article.)

be statically recrystallized grains that recrystallize during cooling after hot deformation, as the size and volume fraction of statically recrystallized grains would increase at a higher strain rate, where the flow stress before unloading (i.e., the driving force for static recrystallization) is larger than at a lower strain rate. Secondly, the EBSD maps in (b) and (c) show some substructures enclosed by LAGBs within the recrystallized necklace grains, proving that they are dynamically recrystallized grains subjected to further deformation up to a strain of 0.8.

The rarely occurring course of necklace formation in BCC Fe-Al-based alloys has been reported only to a limited extent to the authors' knowledge. In the following section, two possible mechanisms for recrystallization are discussed, which depend on whether the original grain boundaries are occupied by Laves phase particles, or whether they are free of particles.

DRX mechanism at the boundaries containing large Laves phase particles – Some recrystallized grains are situated around Laves phase particles close to the grain boundary regions containing a cluster of large particles, as shown in Figs. 4(a)–(d) and S2 for a different area of examination, indicating particle-stimulated nucleation (PSN) [23]. Coarse Laves phase particles likely induce heterogeneous deformation and a high degree of local lattice curvature in their vicinity due to the strain incompatibility between particles and matrix. As a result, deformation zones, including complex dislocation structures, form around the particles, as shown by the Kernel average misorientation (KAM) map in Fig. 4(e). During hot deformation, such particle-related deformation zones are favorable nucleation sites for recrystallizing grains. In the present study, grain orientation spread (GOS) was used as a metric to

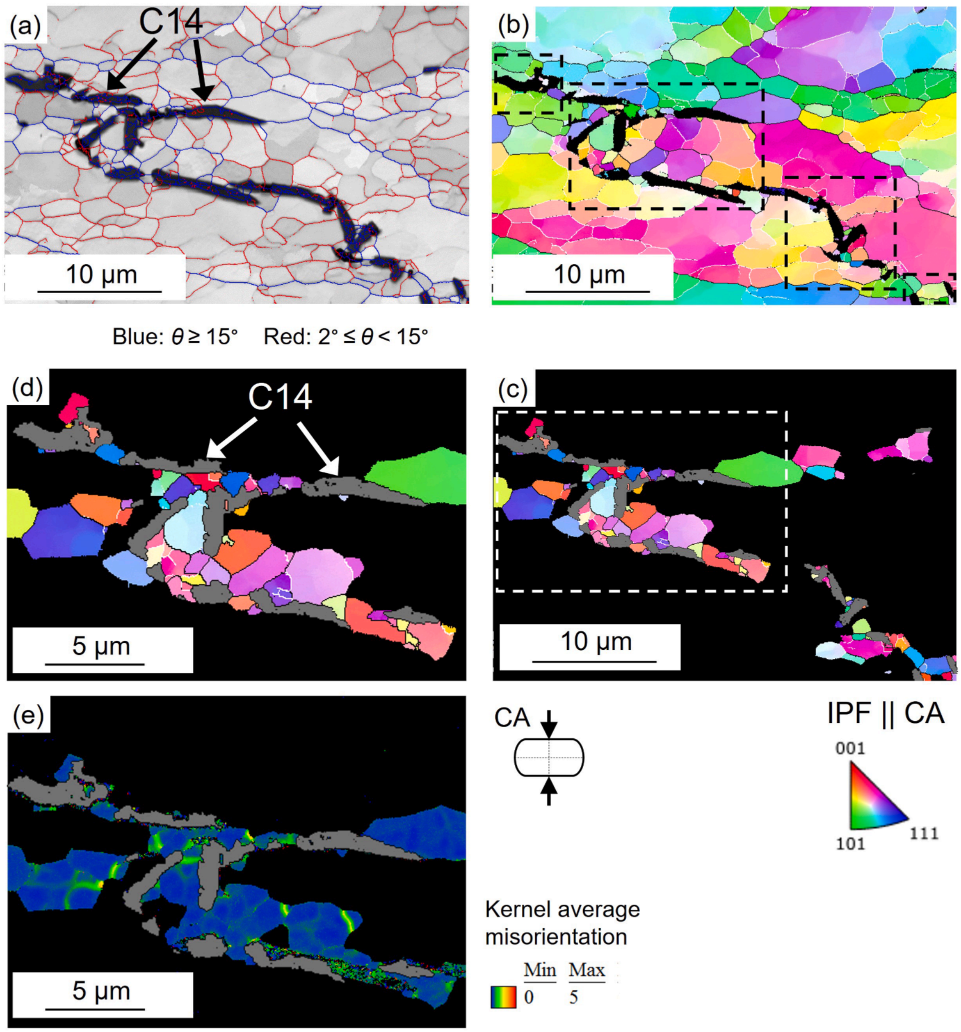

Fig. 4. IQ map (a) and IPF map (b) parallel to the compression axis (CA) showing recrystallized grains (dash squares) nucleated preferentially around C14 particles (black in the maps) in a specimen hot compressed at 900 °C with a strain rate of 1 s^{-1} up to a strain of 0.8, recrystallized grains around the particles separated using the criterion GOS $\leq$ 2° (c), an enlargement of the region in (c) outlined by a white square (d), and Kernel average misorientation (KAM) map showing the substructures within the recrystallized grains (e). The red and blue lines in the IQ map mark LAGBs with misorientations (θ), 2° $\leq \theta <$ 15° and HAGBs with $\theta \geq$ 15°, respectively. The LAGBs and HAGBs are marked by white and black colors in IPF maps. (For interpretation of the references to colour in this figure legend, the reader is referred to the web version of this article.)

distinguish recrystallized grains from unrecrystallized parent grains in the EBSD microstructures [24]. The grains with a GOS $\leq$ 2° were considered recrystallized, and those with a GOS > 2° were considered unrecrystallized [25–27]. The GOS and KAM maps of the recrystallized grains in 4(c-e) show some LAGBs and substructures within the recrystallized grains, indicating that they formed dynamically during deformation and were subjected to further deformation as the imposed deformation proceeds.

Direct observations confirm the weak dominance of a classical nucleation mechanism of recrystallization by bulging of original grain boundaries surrounding the coarse Laves particles, suggesting that particles effectively pin boundary migration. It is worth mentioning that PSN is more pronounced when a cluster of large Laves particles, rather than a single small particle, is located close to the GBs. PSN has been reported as an effective nucleation mechanism for recrystallization in particle-containing FCC [28,29] and BCC materials, including ferritic stainless steel [30] and Fe_3Al-based alloys [31].

DRX mechanism at the boundaries free from the particles – The dominant mechanism by which the first layer of recrystallized necklace grains forms near the particle-free original GBs is the strain-induced bulging of original GBs, as indicated by arrows in Fig. 5(a). The dislocations accumulate at the original GBs during deformation, and the dislocation storage rate probably depends on grain orientation and differs in the boundary regions. The difference in dislocation content (stored energy) on opposite sides of the GB provides the driving force for SIBM [3]. On its concave side, the bulging boundary is joined to the adjacent grain by an array of dislocations or low-angle boundaries, as marked by white lines in Fig. 5(a). As the imposed deformation proceeds, the misorientation of such LAGBs will gradually increase, resulting in equiaxed recrystallized grains surrounded by HAGBs. A characteristic feature of this mechanism is that the new grains have similar orientations to the adjacent parent grains from which they were formed. To verify the mechanism, recrystallized grains were separated from the unrecrystallized parent grains using the GOS $\leq$ 2° criterion, and their orientations were compared. Inverse pole figure (IPF) maps for the unrecrystallized and recrystallized volumes in the specimen hot-compressed to a true strain of 0.8 at 900 °C / 0.0013 s^{-1} are shown in Fig. 5(b) and (c). The IPF direction is parallel to the compression axis (CA). Deformed (unrecrystallized) prior grains surrounded by the necklace grains are elongated in directions perpendicular to the CA and show internal misorientations, which appear as color changes within the grains in the IPF map. The deformed grains preferentially exhibit ⟨001⟩ orientations parallel to the CA (Fig. 5b). The recrystallized grains mostly have orientations close to the orientation of the neighboring parent grains, i.e., ⟨001⟩ orientations parallel to the CA (Fig. 5c). This similarity indicates the orientation coherency of the few first necklace grains with the deformed matrix, verifying the SIBM and bulging mechanism for the first recrystallized grains. It is worth mentioning that bulging is moderate in the alloy studied (and generally in the BCC materials), where dynamic dislocation recovery occurs readily, and serrated GBs, as found in the FCC materials [4], are not usually observed.

After the formation of the first layer of recrystallized grains at the

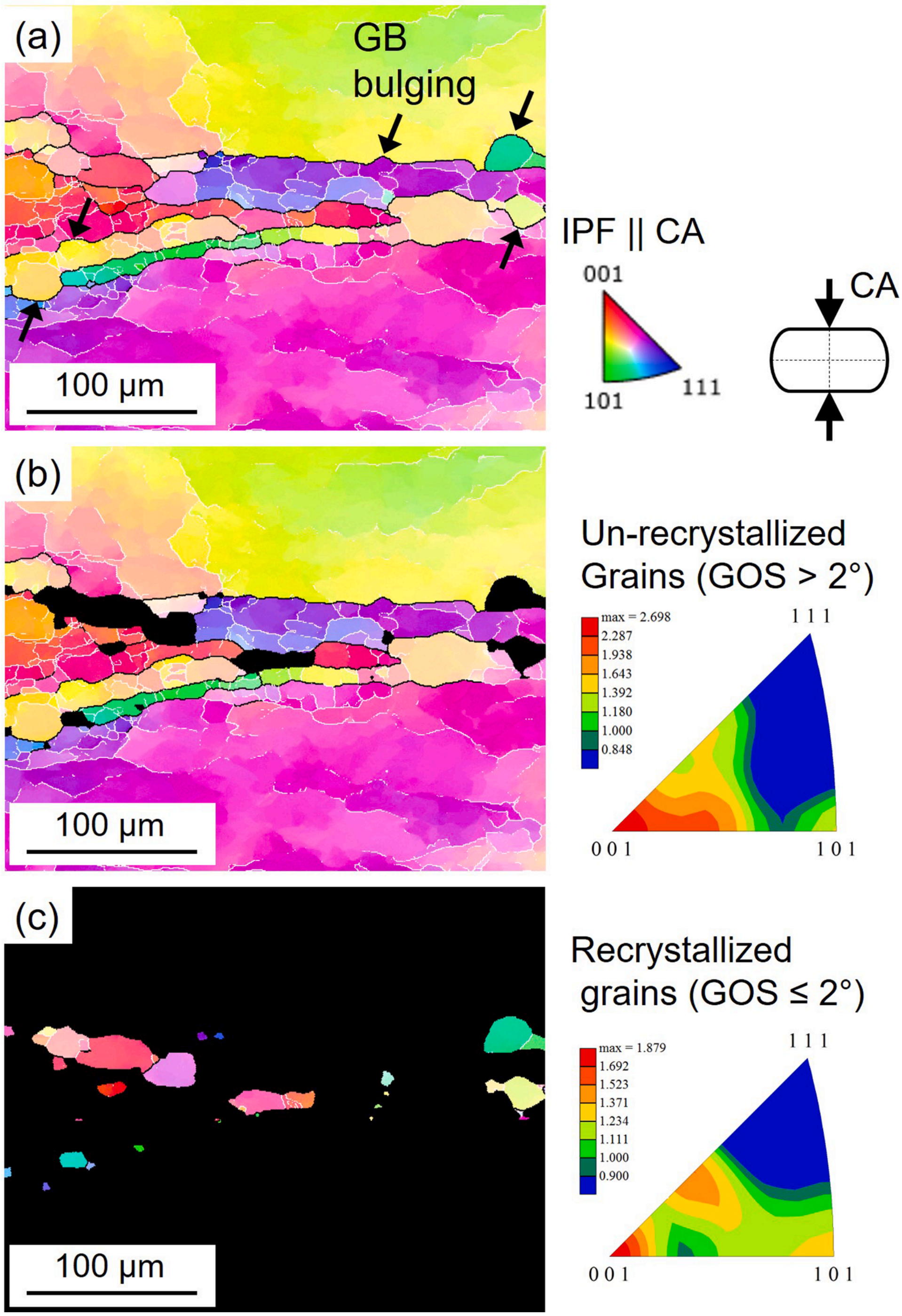

Fig. 5. EBSD-IPF map around a grain boundary region lacking the Laves phase particles showing the bulging of the original grain boundary (indicated by arrows) (a), and IPF maps of the unrecrystallized (b) and recrystallized (c) volumes showing the orientation coherence of the few first necklace grains with the deformed matrix in the Fe-25Al-1.5Ta specimen hot compressed at 900 °C / 0.0013 s^{-1} up to a true strain of 0.8. Unrecrystallized and recrystallized volumes were separated using the GOS criterion (GOS > 2° - unrecrystallized and GOS ≤ 2° - recrystallized). The maps correspond to orientations parallel to the compression axis (CA). The CA is vertical. The white and black lines mark low-angle grain boundaries with misorientations (θ), 2° ≤ θ < 15° and high-angle grain boundaries with θ ≥ 15°, respectively.

original boundaries, the expansion of the necklace volume into the deformed grains possibly proceeds through the formation of low-angle GBs at the interface between the original deformed grains and the finer recrystallized grains, as marked by red lines in Fig. 3(b) and (c), due to strain incompatibility at the interface. These LAGBs decorating the necklace layers will eventually transform into HAGBs with increasing strain, forming the subsequent layers of necklace grains. A similar mechanism has been proposed for the HfNbTaTiZr BCC high-entropy alloy, where the necklace structures expand into the deformed volume by forming subgrains and their evolution into grains [32].

The final key point is that the B2 ordering can affect the recovery and recrystallization behaviors; however, these effects are weak because the B2 is insignificant at the deformation temperature, as confirmed by high-temperature X-ray results. Dislocation motions during deformation in the A2-disordered αFe matrix can be inhibited by B2-ordered FeAl cluster domains [33] dispersed within the A2 matrix. A strong interaction of the dislocations with the disorder-order interface hinders the annihilation of dislocations and their rearrangement into subgrains [1]. Therefore, DRV may be impeded, dislocation pile-ups form, and the stored energy increases. Consequently, the driving force for DRX rises, and the dislocation density can reach the critical value for the onset of DRX. In addition, the B2 superlattice is more difficult to deform than the A2 due to the low mobility of superdislocations and the difficulty of cross slip. Deformation mechanisms based on self-diffusion are also hindered by the ordering effects in B2 [34].

In summary, the present study proposes two possible mechanisms for dynamic recrystallization in BCC Fe-Al-Ta alloys depending on whether the original grain boundaries are occupied by coarse particles of the Laves phase or whether they are free of particles. The Laves phase particles may act as nucleation sites during the initiation of recrystallization by a particle-stimulated nucleation mechanism at the boundaries containing the particles. In contrast, the bulging of original grain boundaries occurs at the boundaries where particles are missing. The presence of the B2-ordered FeAl phase at deformation temperature can also favor recrystallization by hindering recovery. Nevertheless, the B2 ordering seems to be insignificant at the deformation temperature; therefore, its effects on recovery and recrystallization are not dominant.

The results of this study promote the understanding of the essential mechanisms of dynamic recrystallization in particle-reinforced materials, particularly in BCC metals and alloys.

Funding

This research did not receive any specific grant from funding agencies in the public, commercial, or not-for-profit sectors.

Declaration of Competing Interest

The authors declare that they have no known competing financial interests or personal relationships that could have appeared to influence the work reported in this paper.

Acknowledgments

A. Emdadi acknowledges Access e.V. Tech Center (Aachen, Germany) for the investment casting and the Chair of Hybrid Manufacturing (FHF) at BTU Cottbus-Senftenberg for compression tests.

Supplementary materials

Supplementary material associated with this article can be found, in the online version, at doi:10.1016/j.scriptamat.2023.115705.

References

[1] F.J. Humphreys, M. Hatherly, Recrystallization and Related Annealing Phenomena, Elsevier, 2012.
[2] H.K. Zhang, H. Xiao, X.W. Fang, Q. Zhang, R.E. Logé, K. Huang, A critical assessment of experimental investigation of dynamic recrystallization of metallic materials, Mater. Des. 193 (2020), 108873, https://doi.org/10.1016/j.matdes.2020.108873.
[3] J.E. Bailey, P.B. Hirsch, The recrystallization process in some polycrystalline metals, Proc. R. Soc. Lond. A 267 (1962) 11–30, https://doi.org/10.1098/rspa.1962.0080.
[4] D. Ponge, G. Gottstein, Necklace formation during dynamic recrystallization: mechanisms and impact on flow behavior, Acta Mater. 46 (1998) 69–80, https://doi.org/10.1016/S1359-6454(97)00233-4.
[5] R.D. Doherty, D.A. Hughes, F.J. Humphreys, J.J. Jonas, D.J. Jensen, M.E. Kassner, W.E. King, T.R. McNelley, H.J. McQueen, A.D. Rollett, Current issues in recrystallization: a review, Mater. Sci. Eng. A 238 (1997) 219–274, https://doi.org/10.1016/S0921-5093(97)00424-3.
[6] B. Voyzelle, J.D. Boyd, High-temperature deformation behaviour of Fe_3Al, Mater. Sci. Eng. A 258 (1998) 243–248, https://doi.org/10.1016/S0921-5093(98)00940-X.
[7] R. Łyszkowski, J. Bystrzycki, Hot deformation and processing maps of an Fe_3Al intermetallic alloy, Intermetallics 14 (2006) 1231–1237, https://doi.org/10.1016/j.intermet.2005.12.014.
[8] R.S. Sundar, R.G. Baligidad, Y.V.R.K. Prasad, D.H. Sastry, Processing of iron aluminides, Mater. Sci. Eng. A 258 (1998) 219–228, https://doi.org/10.1016/S0921-5093(98)00937-X.
[9] A. Emdadi, I. Sizova, M. Bambach, U. Hecht, Hot deformation behavior of a spark plasma sintered Fe-25Al-1.5Ta alloy with strengthening Laves phase, Intermetallics 109 (2019) 123–134, https://doi.org/10.1016/j.intermet.2019.03.017.
[10] A. Emdadi, H. Michels, M. Tovar, Hot workability investigation of an Fe-Al-Ta alloy using deformation processing maps, Metals 13 (2023) 1195, https://doi.org/10.3390/met13071195.
[11] A. Emdadi, S. Bolz, F. Jensch, M. Tovar, S. Weiß, On the hot deformation of a Fe-Al-Ta iron aluminide prepared via laser powder bed fusion, Crystals 13 (2023) 627, https://doi.org/10.3390/cryst13040627.
[12] M. Wang, C. Sun, M.W. Fu, Z. Liu, C. Wang, Microstructure and microtexture evolution of dynamic recrystallization during hot deformation of a nickel-based superalloy, Mater. Des. 188 (2020), 108429, https://doi.org/10.1016/j.matdes.2019.108429.
[13] K. Huang, R.E. Logé, A review of dynamic recrystallization phenomena in metallic materials, Mater. Des. 111 (2016) 548–574, https://doi.org/10.1016/j.matdes.2016.09.012.
[14] T. Sakai, A. Belyakov, R. Kaibyshev, H. Miura, J.J. Jonas, Dynamic and post-dynamic recrystallization under hot, cold and severe plastic deformation conditions, Prog. Mater. Sci. 60 (2014) 130–207, https://doi.org/10.1016/j.pmatsci.2013.09.002.
[15] N. Tsuji, Y. Matsubara, Y. Saito, Dynamic recrystallization of ferrite in interstitial free steel, Scr. Mater. 37 (1997) 477–484, https://doi.org/10.1016/S1359-6462(97)00123-1.
[16] N. Tsuji, Y. Matsubara, Y. Saito, T. Maki, Occurrence of dynamic recrystallization in ferritic iron, J. Jpn. Inst. Met. 62 (1998) 967–976, https://doi.org/10.2320/jinstmet1952.62.10_967.
[17] G. Glover, C.M. Sellars, Recovery and recrystallization during high temperature deformation of α-iron, Metall. Trans. 4 (1973) 765–775, https://doi.org/10.1007/BF02643086.
[18] O.N. Senkov, J.M. Scott, S.V. Senkova, F. Meisenkothen, D.B. Miracle, C. F. Woodward, Microstructure and elevated temperature properties of a refractory TaNbHfZrTi alloy, J. Mater. Sci. 47 (2012) 4062–4074, https://doi.org/10.1007/s10853-012-6260-2.
[19] R.R. Eleti, T. Bhattacharjee, A. Shibata, N. Tsuji, Unique deformation behavior and microstructure evolution in high temperature processing of HfNbTaTiZr refractory high entropy alloy, Acta Mater. 171 (2019) 132–145, https://doi.org/10.1016/j.actamat.2019.04.018.
[20] F. Dong, Y. Yuan, W. Li, Y. Zhang, P.K. Liaw, X. Yuan, H. Huang, Hot deformation behavior and processing maps of an equiatomic MoNbHfZrTi refractory high entropy alloy, Intermetallics 126 (2020), 106921, https://doi.org/10.1016/j.intermet.2020.106921.
[21] Z. Yu, B. Xie, Z. Zhu, B. Xu, M. Sun, High-temperature deformation behavior and processing maps of a novel AlNbTi3VZr1.5 refractory high entropy alloy, J. Alloy. Compd. 912 (2022), 165220, https://doi.org/10.1016/j.jallcom.2022.165220.
[22] R.D. Pütz, D. Zander, The role of (Fe,Al)2Nb Laves phase on the high temperature oxidation behaviour of intermetallic Fe–26Al–4Nb iron aluminide, Intermetallics 162 (2023), 108002, https://doi.org/10.1016/j.intermet.2023.108002.
[23] F.J. Humphreys, The nucleation of recrystallization at second phase particles in deformed aluminium, Acta Metall. 25 (1977) 1323–1344, https://doi.org/10.1016/0001-6160(77)90109-2.
[24] F. Wagner, N. Allain-Bonasso, S. Berbenni, D.P. Field, On the use of EBSD to study the heterogeneity of plastic deformation, Mater. Sci. Forum 702-703 (2011) 245–252, https://doi.org/10.4028/www.scientific.net/MSF.702-703.245.
[25] Y. Chen, L. Jin, J. Dong, Z. Zhang, F. Wang, Twinning effects on the hot deformation behavior of AZ31 Mg alloy, Mater. Charact. 118 (2016) 363–369, https://doi.org/10.1016/j.matchar.2016.06.014.
[26] C.K. Yan, A.H. Feng, S.J. Qu, G.J. Cao, J.L. Sun, J. Shen, D.L. Chen, Dynamic recrystallization of titanium: effect of pre-activated twinning at cryogenic temperature, Acta Mater. 154 (2018) 311–324, https://doi.org/10.1016/j.actamat.2018.05.057.
[27] S. Irukuvarghula, H. Hassanin, C. Cayron, M.M. Attallah, D. Stewart, M. Preuss, Evolution of grain boundary network topology in 316 L austenitic stainless steel during powder hot isostatic pressing, Acta Mater. 133 (2017) 269–281, https://doi.org/10.1016/j.actamat.2017.04.068.
[28] M. Ferry, F.J. Humphreys, The deformation and recrystallization of particle-containing $\{011\}\langle 100\rangle$ aluminium crystals, Acta Mater. 44 (1996) 3089–3103, https://doi.org/10.1016/1359-6454(95)00432-7.
[29] O. Engler, X.W. Kong, P. Yang, Influence of particle stimulated nucleation on the recrystallization textures in cold deformed Al-alloys Part I–Experimental observations, Scr. Mater. 37 (1997) 1665–1674, https://doi.org/10.1016/S1359-6462(97)00315-1.
[30] R.P. de Siqueira, H.R.Z. Sandim, D. Raabe, Particle stimulated nucleation in coarse-grained ferritic stainless steel, Metall. Mater. Trans. A 44 (2013) 469–478, https://doi.org/10.1007/s11661-012-1408-x.
[31] S. Kobayashi, C. Zambaldi, D. Raabe, Orientation dependence of local lattice rotations at precipitates: example of κ-Fe_3AlC carbides in a Fe3Al-based alloy, Acta Mater. 58 (2010) 6672–6684, https://doi.org/10.1016/j.actamat.2010.08.030.
[32] R.R. Eleti, A.H. Chokshi, A. Shibata, N. Tsuji, Unique high-temperature deformation dominated by grain boundary sliding in heterogeneous necklace structure formed by dynamic recrystallization in HfNbTaTiZr BCC refractory high entropy alloy, Acta Mater. 183 (2020) 64–77, https://doi.org/10.1016/j.actamat.2019.11.001.
[33] A.M. Balagurov, I.A. Bobrikov, S.V. Sumnikov, I.S. Golovin, Antiphase domains or dispersed clusters? Neutron diffraction study of coherent atomic ordering in Fe_3Al-type alloys, Acta Mater. 153 (2018) 45–52, https://doi.org/10.1016/j.actamat.2018.04.015.
[34] S. Divinski, Defects and diffusion in ordered compounds, in. Handbook of Solid State Diffusion, Elsevier, 2017, pp. 449–517. Volume 1.